Available online at www.sciencedirect.com
ScienceDirect
Biomaterials 29 (2008) 161–171
Biomaterials
www.elsevier.com/locate/biomaterials

Hybrid bone implants: Self-assembly of peptide amphiphile nanofibers within porous titanium

Timothy D. Sargeant[a], Mustafa O. Guler[b], Scott M. Oppenheimer[a], Alvaro Mata[b], Robert L. Satcher[c], David C. Dunand[a], Samuel I. Stupp[d,*]

[a]Department of Materials Science and Engineering, Northwestern University, Evanston, IL 60208-3108, USA
[b]Institute for Bionanotechnology for Medicine, Northwestern University, Chicago, IL 60611-2875, USA
[c]Feinberg School of Medicine, Northwestern University, Chicago, IL 60611, USA
[d]Department of Materials Science and Engineering, Department of Chemistry, Feinberg School of Medicine, Northwestern University, Evanston, IL 60208-3108, USA

Received 9 July 2007; accepted 17 September 2007
Available online 23 October 2007

Abstract

Over the past few decades there has been great interest in the use of orthopedic and dental implants that integrate into tissue by promoting bone ingrowth or bone adhesion, thereby eliminating the need for cement fixation. However, strategies to create bioactive implant surfaces to direct cellular activity and mineralization leading to osteointegration are lacking. We report here on a method to prepare a hybrid bone implant material consisting of a Ti–6Al–4V foam, whose 52% porosity is filled with a peptide amphiphile (PA) nanofiber matrix. These PA nanofibers can be highly bioactive by molecular design, and are used here as a strategy to transform an inert titanium foam into a potentially bioactive implant. Using scanning electron microscopy (SEM) and confocal microscopy, we show that PA molecules self-assemble into a nanofiber matrix within the pores of the metallic foam, fully occupying the foam's interconnected porosity. Furthermore, the method allows the encapsulation of cells within the bioactive matrix, and under appropriate conditions the nanofibers can nucleate mineralization of calcium phosphate phases with a Ca:P ratio that corresponds to that of hydroxyapatite. Cell encapsulation was quantified using a DNA measuring assay and qualitatively verified by SEM and confocal microscopy. An in vivo experiment was performed using a bone plug model in the diaphysis of the hind femurs of a Sprague Dawley rat and examined by histology to evaluate the performance of these hybrid systems after 4 weeks of implantation. Preliminary results demonstrate de novo bone formation around and inside the implant, vascularization around the implant, as well as the absence of a cytotoxic response. The PA–Ti hybrid strategy could be potentially tailored to initiate mineralization and direct a cellular response from the host tissue into porous implants to form new bone and thereby improve fixation, osteointegration, and long term stability of implants.
© 2007 Elsevier Ltd. All rights reserved.

Keywords: Tissue engineering; Self-assembly; Bone; Ti–6Al–4V; Foam; MC3T3-E1

1. Introduction

The lifetime of orthopaedic implants is limited primarily by implant loosening, a result of interfacial breakdown and stress shielding [1]. In past clinical practice, fixation of implants has primarily been achieved via screws and bone cements [2]. While initial stability is adequately realized, cement degradation over time or screw loosening eventually lead to implant instability and required surgical revision. Furthermore, implant materials that are much stiffer than bone, e.g., titanium, stainless steel, and cobalt alloys, often lead to stress shielding and subsequent resorption of surrounding bone [3,4]. The current approach of creating porous surfaces on implants attempts to improve fixation, but does not solve the issue of stiffness mismatch. A strategy addressing both problems is to use a porous metallic implant, which allows for the ingrowth of bone to achieve improved fixation and also reduces the Young's modulus of the implant material to better match that of bone [5–10].

*Corresponding author. Fax: +1 847 491 3010.
E-mail address: s-stupp@northwestern.edu (S.I. Stupp).

0142-9612/$ - see front matter © 2007 Elsevier Ltd. All rights reserved.
doi:10.1016/j.biomaterials.2007.09.012

Prior work has shown that metallic scaffolds with pores that are either isolated (closed to the surface) or interconnected (usually open to the surface) can be fabricated with biomedical alloys, including commercially pure titanium (CP–Ti) [11] the alloy Ti–6Al–4V [12–14], and near-equiatomic nickel–titanium alloy (NiTi) [15,16]. Commonly used for bone implants, the Ti–6Al–4V alloy can be foamed by solid-state expansion of argon to a fully open porosity of approximately 50% [17]. This allows for tissue ingrowth as well as considerable elastic modulus reduction, reducing risks of bone resorption due to stiffness mismatch. However, these CP–Ti and Ti–6Al–4V foams remain bioinert at best, without direct capacity to influence cell behavior or encourage bone formation.

There has been recent interest on the design of surfaces on the nanoscale for cell signaling [18–21]. The Stupp laboratory has developed a system of peptide amphiphile (PAs) molecules that self-assemble in aqueous solutions under the appropriate conditions to create high aspect ratio nanofibers that can form a self-supporting gel at low molar percent (10 mM) [22,23]. Self-assembly can be triggered by charge screening via changes in pH or the addition of multi-valent ion or charged molecules. Our PAs are designed such that when self-assembly occurs, a bioactive epitope can be presented in high density on the periphery of the nanofiber. This portion of the PA can be designed with a variety of biologically relevant epitopes without disrupting the self-assembling properties, allowing for the creation of nanofibers that can present an array of epitopes for cellular attachment, signaling, or biomolecule binding [23–25]. As a result, we are able to create an artificial matrix with the advantage of being able to signal host tissue.

We report here on the creation of a bioactive hybrid bone implant consisting of a Ti–6Al–4V foam filled with a PA nanofiber matrix produced by in-situ self-assembly within the foam. We also describe a new method for cell encapsulation within these hybrids, which is desirable to enhance the post-operative recovery associated with cement-free skeletal implants, by increasing cellular proliferation and mineralization, both within the implant and at the implant–tissue interface.

2. Materials and methods

All chemical reagents, unless otherwise noted, were purchased from Sigma-Aldrich (St. Louis, MO). Solvents were purchased from Fisher Scientific (Hanover Park, IL). Amino acids were purchased from EMD Biosciences (San Diego, CA). Cellular medium components were purchased from Invitrogen (Carlsbad, CA) and other cell culture supplies from VWR (West Chester, PA). pEGFP-N1 vector was generously provided by Dr. Earl Cheng (Children's Memorial Hospital, Chicago, IL).

2.1. Ti–6Al–4V foam processing

Procedures established previously for superplastic foaming of CP–Ti and Ti–6Al–4V were followed [11,26–29]. Pre-alloyed Ti–6Al–4V powders (Starmet Corporation) with a particle size range of 149–177 μm were poured in a mild-steel can which was weld-sealed after being evacuated and backfilled with 330 kPa of 99.999% pure argon gas. The can containing the gas and powders was then densified in a hot isostatic press (HIP) for 4 h at 950 °C and at a pressure of 100 MPa. The steel can was then removed and the Ti–6Al–4V billet (10 mm diameter and 10 mm height) was annealed for 180 h in a high-vacuum furnace (residual gas pressure: 10^{-5} mTorr) to let the entrapped argon, present as small, isolated spherical pores, expand within the solid Ti–6Al–4V matrix. Temperature was continuously cycled between 890 and 1030 °C with an 8 min period, so as to induce transformation superplasticity within the Ti–6Al–4V matrix, which has been previously demonstrated to enhance the foaming rate as compared to isothermal annealing [11,26,27,29]. The total porosity of the foamed billet was determined by the water–displacement Archimedes method and the closed porosity by helium pycnometry.

The foamed Ti–6Al–4V billet was cut into 1–2 × 4 × 4 mm^3 samples using a diamond saw with oil lubrication, which were ultrasonically cleaned with dichloromethane, acetone, and water for 15 min each. To remove metal smearing into the external pores from cutting, the samples were exposed to an aqueous solution of 0.25% HF and 2.5% HNO_3 for 45 min. After repassivation with 40% HNO_3 for 30 min, samples were repeatedly rinsed in ultrapure water and dried in a desiccator.

2.2. Peptide amphiphile synthesis and preparation

PA were synthesized using methods previously described [25,30]. Solid phase peptide synthesis (SPPS) was performed using Rink amide MBHA resin with standard 9-Fluorenylmethoxycarbonyl (Fmoc) protected amino acids in *N,N*-dimethylformamide (DMF), diisopropylethylamine (DIEA) and 2-(1H-Benzotriazol-1-yl)-1,1,3,3-tetramethyluronium hexafluorophosphate (HBTU). To create the branched PA architecture, palmitic acid was first coupled to the ε-amine on a lysine to create a hydrophobic tail group. The peptide sequence was then synthesized using orthogonal protecting group chemistry. Selective deprotection of Fmoc, Boc, and 4-methyl trityl (Mtt) protecting groups allowed for control over the design of the PA. After synthesis, the PA was cleaved from the resin using TFA: triisopropyl silane (TIS): water (95:2.5:2.5), precipitated with ice-cold ether, solubilized in water, and dried by lyopholization. The product was then characterized using MALDI-TOF and analytical HPLC.

2.3. Cell culture

Mouse calvarial pre-osteoblastic (MC3T3-E1) cells were cultured under standard tissue culture conditions at 37 °C and 5% CO_2 in Minimum Essential Medium α (MEMα) medium supplemented with 10% fetal bovine serum (FBS), 100 units/mL penicillin and streptomycin, 10 mM β-glycerophosphate, 50 μg/mL ascorbic acid. For confocal imaging, it was desirable to transfect a population of MC3T3-E1 cells with a green fluorescent protein vector to enable fluorescent imaging. This was achieved by plating cells at greater than 90% confluency in antibiotic-free MEMα medium, adding 1 μg pEGFP-N1 vector and 2.3 μL Lipofectamine™ 2000 transfection reagent (Invitrogen) in antibiotic-free MEMα medium without serum, mixing gently and incubating for 24 h at 37 °C. Cells were then passaged and cultured in MEMα medium for 1 day, followed by medium exchange with selection medium consisting of penicillin/streptomycin-free MEMα medium containing 600 μg/mL Geneticin® selective antibiotic (Invitrogen). Cells were cultured in selection medium for 14 days, followed by culturing in maintenance medium, consisting of penicillin/streptomycin-free MEMα medium containing 300 μg/mL Geneticin® selective antibiotic. Cells were then sorted by flow cytometry to obtain a homogeneous population for cell experiments hereon termed GFP-MC3T3-E1 cells. All experiments with GFP-MC3T3-E1 cells were performed using the maintenance medium.

2.4. PA–Ti hybrid preparation

To create PA gels within the Ti–6Al–4V foams, lyophilized PA powder was solubilized in ultrapure water to 2 wt%, pH adjusted to approximately

7, and further diluted to 1 wt% with Dulbecco's phosphate buffered saline (PBS). For the biotinylated PA, FITC-labeled avidin was added in at 1:400 molar ratio. Meanwhile, Ti–6Al–4V foams were autoclave sterilized, and pre-wet via graded soakings starting with 100% ethanol and ending with 100% ultrapure water. The pre-wet Ti–6Al–4V foam samples were then placed in the PA, and agitated on a plate shaker at low speed for 30 min. RGDS PA or S(P) & RGDS PA mixtures were gelled with the addition of 7 μL of 1 M $CaCl_2$ to each sample solution (~85 mM $CaCl_2$ final concentration), while the biotinylated PA was gelled by subjecting the samples to ammonium hydroxide (NH_4OH) vapor to bring the pH up to ~8.5. Following gelation, samples were annealed by incubation at 37 °C and 5% CO_2 for 1.5 h. For cellular assays and in vivo experiments, the excess PA was scraped aseptically from the exterior. These PA nanofiber/Ti–6Al–4V foam hybrids are termed PA–Ti hybrids in the following. For in vitro mineralization, PA–Ti hybrids were incubated at 37 °C and 5% CO_2 in human mesenchymal stem cell osteogenic medium (Lonza) supplemented with 20mM $CaCl_2$ for 7 days. As described below, PA–Ti hybrid samples were characterized by scanning electron microscopy (SEM) and/or confocal microscopy.

2.5. Cell encapsulation

To encapsulate cells within the PA–Ti hybrid a similar procedure was used. Cells were detached from culture plates by trypsinization, counted, and resuspended in PBS without calcium or magnesium at twice the final cell concentration. Lyophilized PA powder was solubilized in 0.1 M ammonium hydroxide to 4 wt%, diluted to 2 wt% with PBS, and pH adjusted to ~7 with 0.1 M HCl. The PA solution was then sterilized by UV radiation for 30 min. Equal volumes of the PA solution and cell suspension were then mixed and aliquoted into a half-area 96-well plate. The pre-wet Ti–6Al–4V foams were again placed in the PA and cell solution, shaken for 30 min, gelled with $CaCl_2$, and annealed for 1.5 h at 37 °C and 5% CO_2. Samples for SEM and confocal microscopy were then cultured overnight in maintenance medium.

2.6. Biological analysis

For cell quantification, PA–Ti hybrid samples were extracted and frozen in liquid nitrogen, lyophilized, and digested in a papain solution [31]. Briefly, samples were incubated in 0.125 mg/mL papain activated with 1.76 mg/mL cysteine in phosphate buffer with EDTA (0.1 M Na_2HPO_4, 0.01 M Na_2EDTA, pH adjusted with 1 N NaOH) for 16 h at 60 °C. Samples were then assayed for dsDNA content using a Quant-iT PicoGreen dsDNA Assay Kit (Molecular Probes) as per protocol. A 5 μL aliquot of digestion solution was incubated with 95 μL of 1X TE and 100 μL of PicoGreen Working Reagent for 5 min and fluorescence was read on a Gemini EM fluorescence/chemiluminescence plate reader with ex/em of 480/520 nm. A standard curve made with calf thymus DNA was used to convert fluorescence to cell number assuming 7.7 pg DNA/cell [32].

PA–Ti hybrid samples with and without cells for SEM and confocal microscopy were extracted and pre-fixed with 1% gluteraldehyde in MEMα on ice for 1 h. Samples were rinsed in PBS for 20 min, and fixed in 2% formaldehyde, 2% gluteraldehyde in 0.1 M cacodylate buffer for 3 h at room temperature and then overnight at 4 °C. Samples were then rinsed in cacodylate buffer for 20 min and dehydrated using a graded series of ethanol. Mineralized PA–Ti hybrid samples for SEM were removed from media and dehydrated in graded ethanol. At this point, all SEM samples were critical point dried, coated with 3 nm Au–Pd, and imaged using a Hitachi S-4500 (Schaumburg, IL) with a cold field emission electron gun at 3 kV with a current of 20 mA or an FEI Quanta ESEM fitted with a Schottky thermal field emission gun and Oxford EDS at 10 kV. A secondary electron detector was used for high-resolution imaging. Alternatively, samples for confocal microscopy were embedded in EmBed-812/ DER 73 (Electron Microscopy Sciences) according to protocol. Briefly, samples were rinsed in propylene oxide for 20 min, followed by 50:50 solution of EMbed-812/ DER 73:propylene oxide overnight, and then straight EMbed-812/ DER 73 with several fresh exchanges. The resin was then cured for 24 h each at 40, 60, and 70 °C. Embedded samples were then sectioned using a diamond saw and mounted on glass slides. Imaging was performed on a Leica Confocal Laser Scanning System inverted microscope (Bannockburn, IL) using an argon laser and driven with Leica Confocal Software.

2.7. In vivo testing

Preliminary in vivo performance of the PA–Ti hybrids was assessed using a rat femoral model. The study utilized 13 animals containing two implants in each hind limb. Surgical procedures and animal care were approved by Northwestern University's Animal Care and Use Committee. PA–Ti hybrids were implanted into 40-week old Sprague Dawley rats obtained from Harlan (Indianapolis, IN) with preoperative weights of approximately 450–500 g. The animals were anesthetized by intraperitoneal injection of Ketamine (100 mg/kg) and Xylazine (5 mg/kg). The femoral diaphysis was approached through a lateral incision in the skin and circumferential stripping of the muscle. Two 2 mm diameter holes were drilled on the diaphysis of the femur through the first cortex. Cylindrical PA–Ti hybrid implants measuring 3 mm in length and 2 mm in diameter were press fit into the holes, which were sufficiently tight to provide adequate fixation of the implants. The muscle and skin were then sutured to close the wound. After 4 weeks, the animals were sacrificed and implants retrieved for histological analysis. Samples were fixed, plastic embedded, and then sectioned with Exakt cutting and grinding equipment (Oklahoma City, OK). Histological samples were stained with either Goldner's Trichrome or methylene blue and basic fuchsin.

3. Results and discussion

3.1. Ti–6Al–4V foam processing

The foamed billet had a total porosity of 52.5% after 180 h of thermal cycle foaming (8 min per cycle from 890 to 1030 °C). A 1 cm cube sample cut from the billet had a total porosity of 52.5% with 14.2% closed porosity. When the pores expand, they merge with each other forming networks which, as they connect to the billet surface, allow for the gas to escape, thus eliminating the driving force for foaming and leading to open porosity. The porosity of 52.5% achieved here is higher than any other value reported in the literature for Ti–6Al–4V foams produced by solid-state expansion at constant temperature: 32% for Kearns et al. after 46 h at 1240 °C [33,34] (or 40% for several days at 1250 °C [34]), 23% for Queheillalt et al. [14] after 10 h at 920 °C and 35–40% for Schwartz et al. [35] after 24 h at 920 °C. The higher porosity achieved here illustrates that transformation superplasticity, produced by thermal cycling conditions, delays pore merging due to fracture of pore walls (leading to the formation of a pore network and eventual escape of gas from the sample), as compared to isothermal, non-superplastic foaming conditions used in the previous studies. It is noteworthy that even though the foams in the latter two studies were faced with dense Ti–6Al–4V sheets (thus preventing escape of gas on two sides of the foam), their porosity remained below that achieved here under superplastic condition. Based on their porosity of 52.5%, the present foam stiffness is calculated as 25 GPa (using a Young's modulus of 110 GPa for Ti–6Al–4V and standard equations linking stiffness with the square of porosity [36]), close to the range of dense

cortical bone (wet at low strain rate, 15.2 GPa; wet at high strain rate, 40.7 GPa [37]).

Fig. 1 shows an SEM micrograph of a polished cross-section of the foam. The mean line intercept is 110 μm, corresponding to a pore diameter of 165 μm, under the assumption that pores are spherical, monosized and unconnected (real pore size differs from this value, given that these assumptions are not fulfilled). It is generally accepted that the optimum pore diameter for bone ingrowth is 150–400 μm [7], although it has been shown that bone can grow into pores as small as 60 μm [38]. The pores in Fig. 1 are jagged and equiaxed, as also observed in previous studies of CP–Ti foams with similar high porosity [27,29], where it was shown that protrusions within the large pores are remnants of the fractured pores walls initially separating small pores that have merged.

3.2. Preparation of the PA–Ti hybrid

Two complementary microscopic techniques were used to characterize the structure of the PA–Ti hybrids. First, SEM was utilized to image the exterior surfaces and the PA nanostructure. Second, confocal microscopy of cross-sectioned samples was performed to characterize study the interior of the PA–Ti hybrids.

SEM images were taken of the bare exterior surface of the Ti–6Al–4 foams (after acid treatment and repassivation) and the PA–Ti hybrids, as shown in Fig. 2. A low magnification image (Fig. 2B) shows the irregular shape of pores in the foam, also visible in the cross-section image in Fig. 3. When the hybrid is created by triggering self-assembly of the PA solution contained within the Ti–6Al–4V foam, the external pores are completely filled with the PA nanofiber matrix, as shown in Fig. 2C and E. Higher magnification images (Fig. 2D and E) reveal very high aspect ratio, self-assembled PA nanofibers forming a complex tangled matrix not only within the larger macroscopic porosity of the Ti–6Al–4V foam, but also as a thin layer on the outer surfaces of the Ti–6Al–4V foam. This may allow implants to have a bioactive matrix within the larger scale pores of the Ti–6Al–4V, but also on their exterior surfaces that come in direct contact with host tissues.

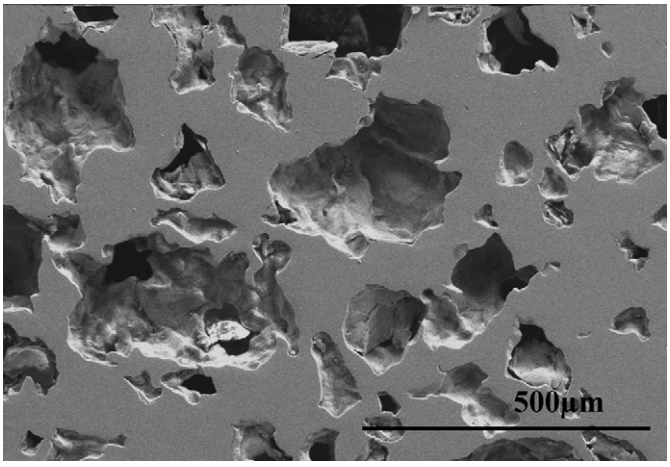

Fig. 1. SEM micrograph of polished, bare Ti–6Al–4V foam in cross-section. The mean line intercept was 110 μm, corresponding to a pore diameter of 165 μm. The pores are irregular in shape and equiaxed, showing no preferential orientation.

Confocal microscopy images were taken of sectioned Ti–6Al–4V foams to evaluate the effectiveness of the PA to self-assemble into a gel matrix within the metallic foam. To be able to image the PA, a biotinylated version of the PA used for SEM and the cell experiments was used in conjunction with FITC-labeled avidin. Given the well-known strong interactions between avidin and biotin [39–41], previous work in the Stupp laboratory has shown this to be a useful method to fluorescently tag PA using FITC-labeled avidin [30]. Fig. 3 shows the chemical structure of the biotinylated PA (A) and the resulting confocal images (B–D). The images shown in Fig. 3B–D are composites of multiple dual-channel overlayed images in order to show the full cross-section of the sample. The first channel measured reflectance (gray) while the second channel measured GFP fluorescence (green). Fig. 3B shows Ti–6Al–4V foam that has been impregnated with a biotinylated PA and FITC-labeled avidin; Fig. 3C shows Ti–6Al–4V foam that has been impregnated with only biotinylated PA; and Fig. 3D shows bare Ti–6Al–4V foam without PA that was embedded with acrylic. All samples were imaged under identical conditions. As expected, there is no observed fluorescence from either the biotinylated PA itself (Fig. 3C) or the foam embedded in acrylic (Fig. 3D). Meanwhile, the FITC-labeled avidin that is bound to the biotinylated PA is clearly visible throughout the entire cross-section, confirming the ability of the PA to penetrate the interconnected porosity of the Ti–6Al–4V foam. Furthermore, since PA was retained within the pores after the five solution exchanges during the embedding procedure, it is very likely that self-assembly of the PA molecules into an entangled matrix had occurred due to successful diffusion of the $CaCl_2$ throughout the thickness of the sample. If the PA would have remained in the unassembled state, the PA would be expected to have been removed during the multiple solution exchanges. While the PA is shown to be present in the entire cross-section, there are several reasons why PA may not be visible in all of the pores. As mentioned earlier, not all the pores are interconnected. Secondly, incomplete infiltration of the resin may have led to PA removal during the sectioning process. Finally, reflectance from the metal made fluorescent imaging difficult. Consequently, it was not possible to obtain a single image that captured the fluorescence all of the pores. To better illustrate the true infiltration, we combined two images to create the composite image shown in Fig. 3B. The presence of the PA covering the exterior (top and bottom) surfaces of the foams is also apparent in the confocal images as previously demonstrated in the SEM images.

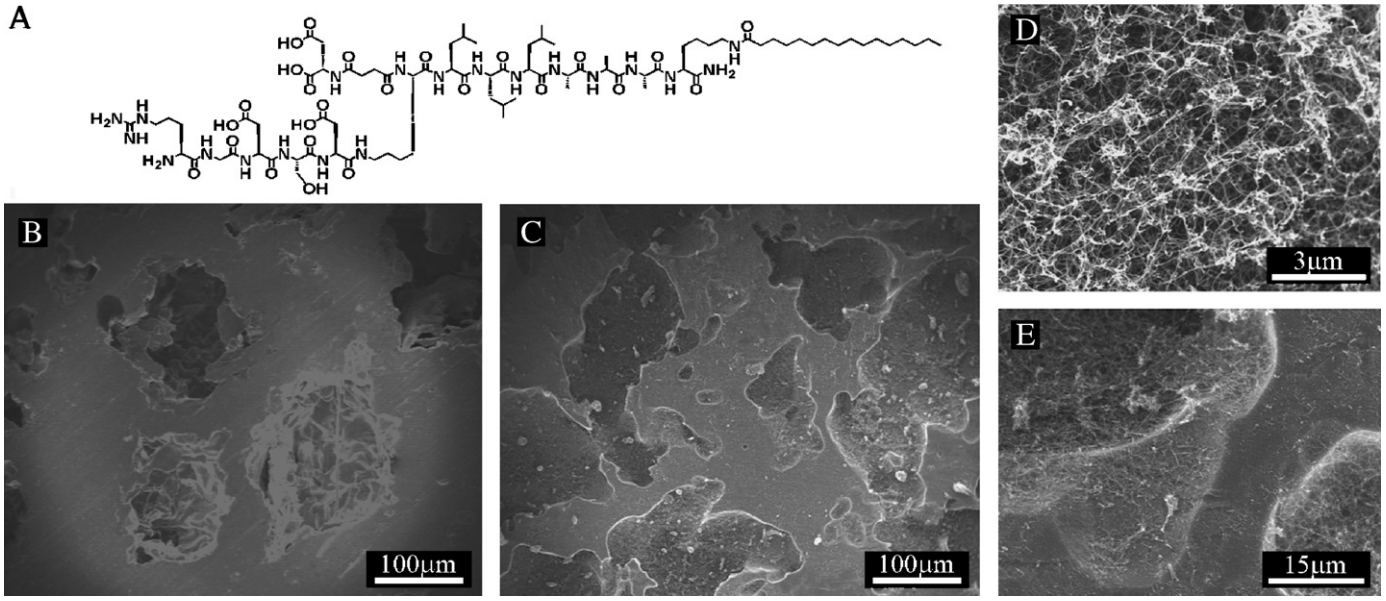

Fig. 2. (A) Chemical structure of the peptide amphiphile (PA) used to infiltrate and fill the pores of the Ti–6Al–4V foam. Scanning electron microscopy (SEM) images of (B) the bare Ti–6Al–4V foam; (C) Ti–6Al–4V foam filled with PA gel; (D) higher magnification of the self-assembled PA nanofibers forming a three-dimensional matrix within the pores; and (E) higher magnification of the PA coating the Ti–6Al–4V foam surface and filling the pores.

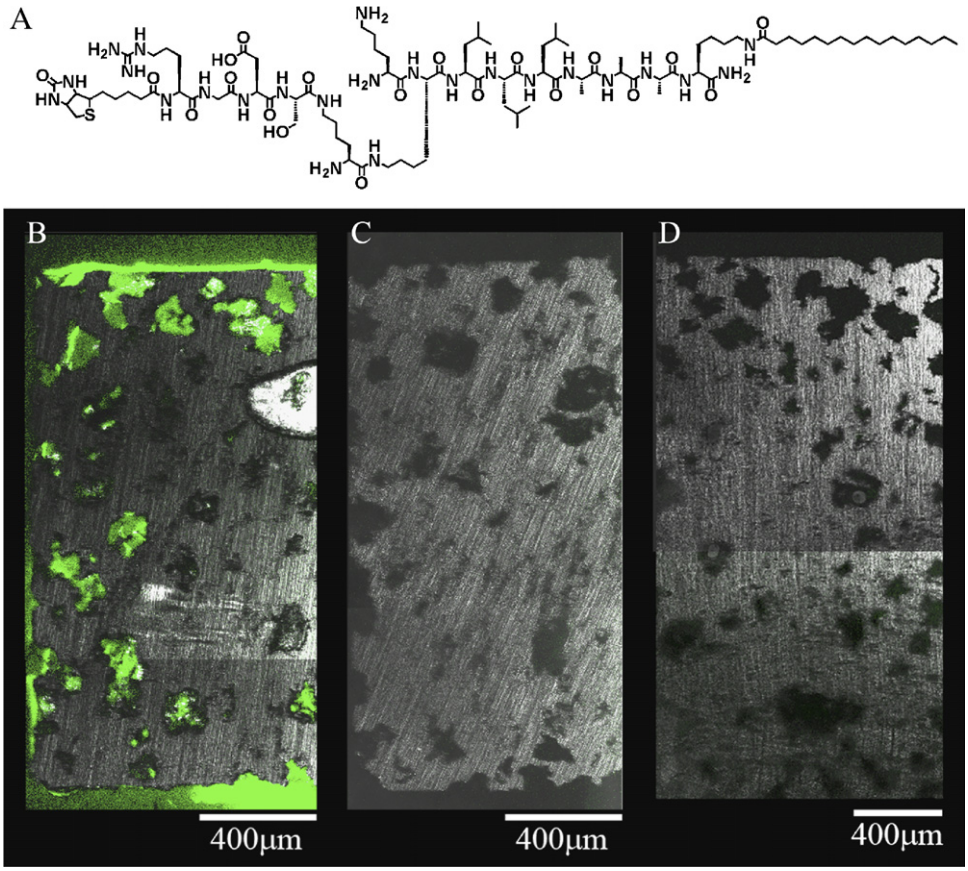

Fig. 3. Chemical structure of the biotinylated PA used for the confocal microscopy without cells (A), and the resulting confocal microscopy images of the biotinylated PA–Ti hybrids embedded in acrylic and cross-sectioned, showing (B) the fluorescence of avidin–FITC bound to biotinylated PA gelled throughout the cross-section of Ti–6Al–4V foam, (C) no fluorescence from a control sample of Ti–6Al–4V foam and biotin–PA without avidin–FITC, and (D) no fluorescence from a second control of Ti–6Al–4V in acrylic without PA.

3.3. Mineralization of the PA matrix

Based on previous results on the mineralization of PAs incorporating a phosphoserine residue [23], we created a mixed PA system with 95 mol % phosphoserine (S(P)) containing PA and 5 mol% RGDS containing PA and used it to create PA–Ti hybrids that might induce mineralization of the nanofibers (PA structures shown in Fig. 4A, B). After incubation of these PA–Ti hybrids for 7 days in medium, samples were evaluated for mineral formation by SEM. As seen in Fig. 4C–E, small spherical structures are observed to have nucleated and grown all along the PA nanofibers. High-resolution imaging reveals that these spherical structures are fairly homogeneous in size and dispersion. Furthermore, due to their location along the fibers, and not in clusters or caught between the nanofibers, it is clear that these are not simply precipitates that have adsorbed onto the nanofibers, but rather they have originated from the nanofibers themselves. Analysis by EDS shows peaks for both calcium and phosphate, and quantification yields a Ca:P ratio of 1.71 ± 0.18. This value is similar to that associated with hydroxyapatite (1.67) based on the formula $Ca_{10}(PO_4)_6(OH)_2$, and is anticipated based on previous work on the mineralization of PAs incorporating the S(P) residue [23].

3.4. Encapsulation of cells within nanofiber matrix of PA–Ti hybrid

Confirmation of the presence of cells encapsulated within the self-assembled PA nanofibers was determined by several approaches. First, a PicoGreen dsDNA assay was utilized to determine the number of cells associated with the PA–Ti hybrid. Secondly, qualitative observation of cells within the hybrids was achieved by confocal microscopy of cross-sectioned samples and SEM imaging of the exterior of the samples. Finally, a live/dead assay was performed to confirm the biocompatibility of the PA gel.

Quantification of the number of cells encapsulated in the PA–Ti hybrids was achieved by utilizing a Quant-iT PicoGreen dsDNA assay kit after 1.5 h of incubation. Cell-encapsulated PA–Ti hybrids were created using PA solutions containing three different cell seeding densities. Five samplings from three to five foams were measured for each seeding density of 5×10^5, 1×10^6, and 5×10^6 cells/mL PA solutions. The samplings were averaged for each foam to determine the cell seeding, and error was set as the standard deviation of these averages. As shown in Fig. 5, the resulting cell population encapsulated within the Ti–6Al–4V foams showed a general increase with increasing initial cell seeding concentrations. A correlation analysis demonstrated a good linear fit ($R^2 = 0.992$) between the initial cell seeding concentration and the resulting number of cells encapsulated within the Ti–6Al–4V foams. This demonstrates that cells can indeed be encapsulated within the PA–Ti hybrids, and that this can be done in a controlled manner.

SEM offered a qualitative method to observe cells encapsulated near the surface of the PA–Ti hybrids. As shown in Fig. 6, encapsulated GFP-MC3T3-E1 cells can be seen within 100 μm from the surface of the sample, attaching and spreading in the PA nanofiber matrix that fills the Ti–6Al–4V foams. Culturing the samples for ~16 h

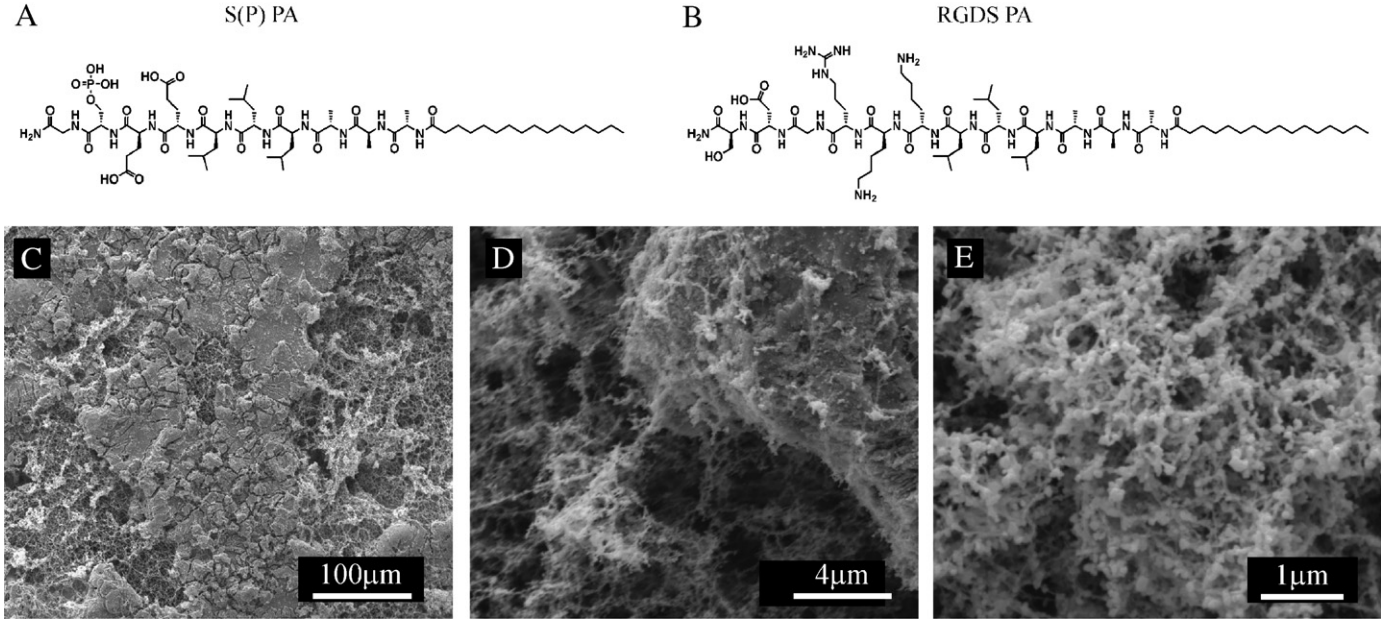

Fig. 4. Chemical structures of the S(P) PA and RGDS PA used to create PA–Ti hybrids for mineralization (A, B). SEM images (C–E) show nanoscale bead-like mineral formation on the PA nanofibers. High magnification images (D–E) show the mineral formation only on the nanofibers, and not on the metal surface, indicating templation on the PA nanofibers. EDS quantification reveals a Ca:P ratio for the mineral as 1.71 ± 0.18, in line with hydroxyapatite.

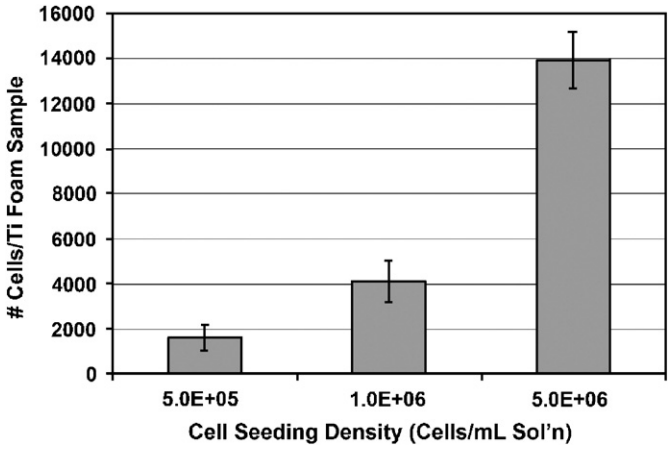

Fig. 5. Quantification of cells encapsulated within PA–Ti hybrids at different seeding densities, showing a direct correlation between seeding density and encapsulated cell number.

provided enough time for the cells to start to exhibit a reaction to their surrounding environment, yet not enough time for proliferation to distort the qualitative observations of the cellular location within the samples. The cells appear stretched in shape with extended processes, and more importantly, we did not observe rounded shapes that may be indicative of apoptosis. The experiments confirmed the presence of cells within the PA–Ti hybrids and their interaction with the surrounding PA matrix.

Fluorescent confocal microscopy was used to qualitatively confirm the presence the cells within the interior PA nanofiber matrix of the PA–Ti hybrids after 1.5 h incubation. Fixed samples were embedded in acrylic and cross-sectioned for observation as described earlier. Fig. 7 shows the two channels measured, reflectance in gray (A) and GFP fluorescence in green (B). Due to the particular angle of the sample and *z*-depth of the cells imaged, reflectance of the metal was also detected by the detector, giving a false fluorescence for the metal. Therefore, the true fluorescence is given by the subtraction of the (A) from (B). It is apparent from these images that the cells are indeed encapsulated within the PA nanofiber matrix as several are observed within the Ti–6Al–4V pore, as indicated with arrows in Fig. 7A, B. Because of the sharp *z*-depth resolution of the confocal microscope, it was determined that the cells are not attached to the pore surface above or below the plane of view, and they are also clearly not in contact with the pore surface within the imaging plane. Therefore, we can conclude that they are suspended within the PA nanofiber matrix. Furthermore, we expect to see individual cells spaced apart because the cells dispersed in solution were effectively entrapped as self-assembly of the nanofiber matrix occurred, minimal time was allowed for cell proliferation or migration, and also because out of plane cells are not visible due to the sharp *z*-depth imaged by confocal microscopy. Together with the SEM images, we can also conclude that the cells measured in the quantification assay are indeed encapsulated throughout the PA–Ti hybrid and not merely adhering to the exterior foam surface.

3.5. In vitro testing of PA–Ti hybrids

To assess any potential cytotoxicity of the PA, a live/dead assay was performed on non-GFP transfected MC3T3-E1 cells encapsulated in just the self-assembled RGDS PA gel. After 5 days of culture, fluorescent optical microscopy was used to qualitatively evaluate the number and morphology of live cells with calcein AM (green) and dead cells with ethidium homodimer (red). As shown in Fig. 8, the vast majority of cells was alive and spread throughout the entire gel, indicating that there was no significant cytotoxic effect. In fact, the cells appeared to survive well in this environment, spreading in the PA nanofiber matrix and not migrating out of the gel. Live/dead was not performed on the PA–Ti hybrids due to the difficulties associated with fluorescent imaging of the opaque foams.

3.6. In vivo testing of PA–Ti hybrids

A preliminary analysis of in vivo performance was carried out for PA–Ti hybrids containing a 95 mol% S(P)/5 mol% RGDS PA mixture (see Fig. 9). Two samples were evaluated by histological analysis and were observed to show similar features. Fig. 10A shows a Goldner's trichrome stained histological image from one of the implants, revealing the growth of new bone from the cortical bone towards the implant that creates a rim of bone encircling the implant in the bone marrow cavity. This new bone is highly mineralized and has the same structure as the cortical bone (CB) with lacunae. Furthermore, bone can be seen forming inside the pores of the implant, where new, unmineralized bone is stained red and mineralized bone is stained green. It is not possible to distinguish between mineralized PA and mineralized matrix deposited by osteoblasts; however, due to the results of the in vitro mineralization, it is reasonable to expect that the PA would begin to mineralize when implanted. Furthermore, the extent of bone formation into the implant demonstrates that the pores are sufficiently interconnected to allow for cellular migration between pores and nutrient diffusion. As shown in Fig. 10B, bone has grown directly against the PA–Ti implant surface. Furthermore, we see evidence of neovascularization around the implant, including the artery shown with red blood cells in the lumen. As observed in the methylene blue and basic fuchsin stained histological image in Fig. 11A, most of the volume of an interior pore can fill in with bone. Fig. 11B shows bone spicules being formed adjacent to the implant in the bone marrow, offering evidence for osteoconduction. The spicule demonstrates a growth front into the PA–Ti hybrid, with collagenous fiber formation and early deposition of bone adjacent to the implant exterior, and bone that is being calcified on

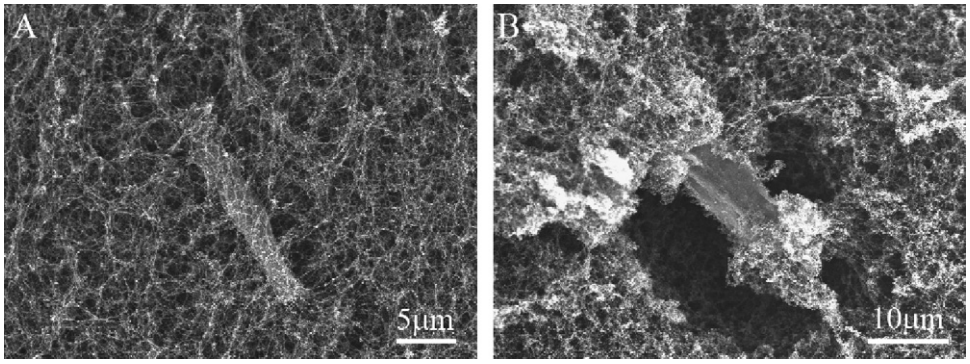

Fig. 6. SEM of GFP-transfected MC3T3-E1 cells encapsulated within PA–Ti hybrids. Cells encapsulated near the surface of the PA gel can be visualized spreading and pulling on the nanofibers presenting the RGDS cellular adhesion motif.

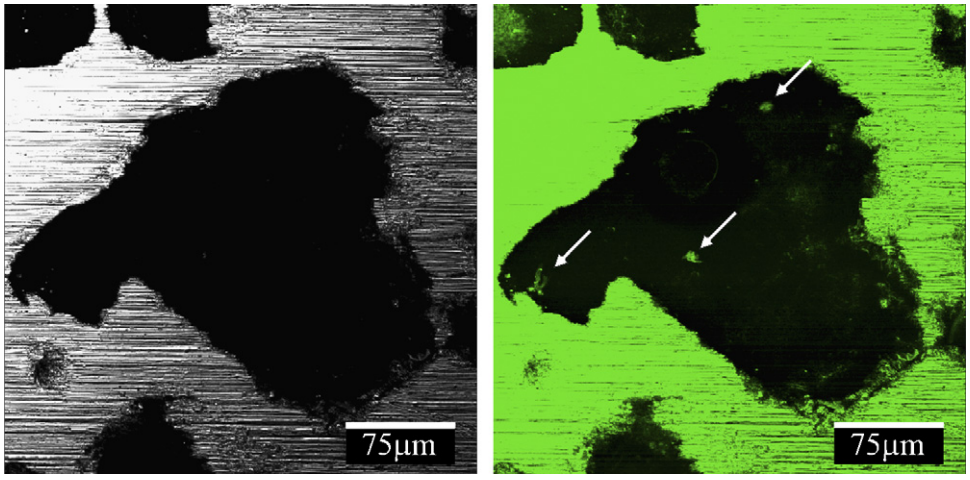

Fig. 7. Confocal microscopy of GFP-transfected MC3T3-E1 cells encapsulated within PA–Ti hybrids (cross-section). Left image is reflectance mode, while right image is fluorescence, showing cell suspended in an interior pore. The metal shows artificial fluorescence due to reflectance at the wavelength collected. The difference between the images is the true fluorescence of the cells, indicated by the arrows.

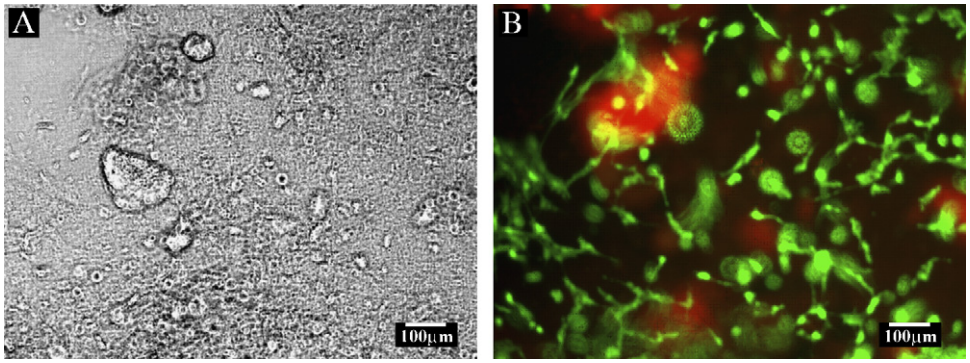

Fig. 8. Optical (A) and fluorescence (B) microscopy images of non-transfected MC3T3-E1 cells encapsulated within the nanofiber matrix of the PA shown in Fig. 2A. Almost all cells fluoresced green due to the conversion of calcein AM to calcein, indicative of live cells. The hazy red areas are background fluorescence due to the interaction of the PA with EthD-1.

the outer layer. The wedge formation at the top of the spicule growing into the pore indicates cellular infiltration by the osteoblasts. The bone marrow appears healthy with intact and viable hematopoietic cells and areas of adipose tissue, and there is no evidence of cytotoxic effects based on the absence of neutrophils. Preliminary analysis of all samples by SEM also indicates that implants are indeed surrounded by bone. A quantitative analysis of the in vivo response using microscopy and histology is beyond the scope of this work and will be reported in a future manuscript.

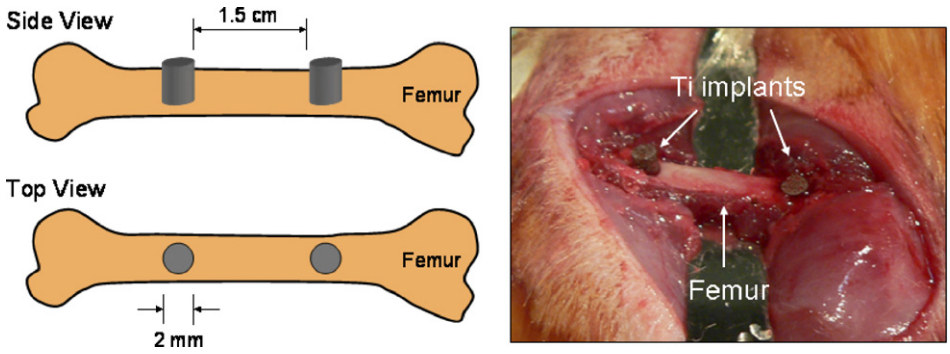

Fig. 9. Image depicts the rat femoral model used to assess the biocompatibility and osteoconductive/inductive potential of the Ti implants. Ti foam implants were positioned inside 2 mm diameter holes that were ~1.5 cm apart.

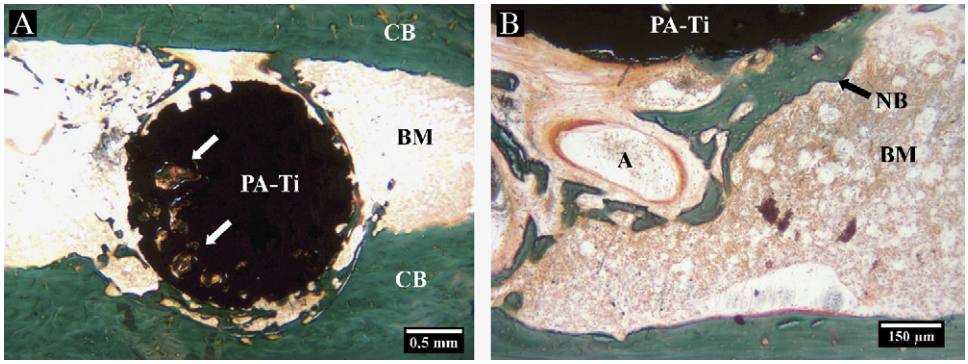

Fig. 10. Images of histological sections of a PA–Ti hybrid implanted in a rat femur after 4 weeks. Non-decalcified, plastic embedded samples were stained with Goldner's Trichrome. When staining bone, green indicates highly mineralized bone; red indicates newly formed, immature bone. As seen in Image A, new, mineralized bone is seen growing from the cortical bone (CM) towards the PA–Ti hybrid in the bone marrow (BM), and infiltrating the open porosity (arrows). Image B shows newly formed, fully mineralized bone adherent to the PA–Ti hybrid exterior. An artery (A) is observed adjacent to the implant, indicating neo-vascularization around the PA–Ti hybrid.

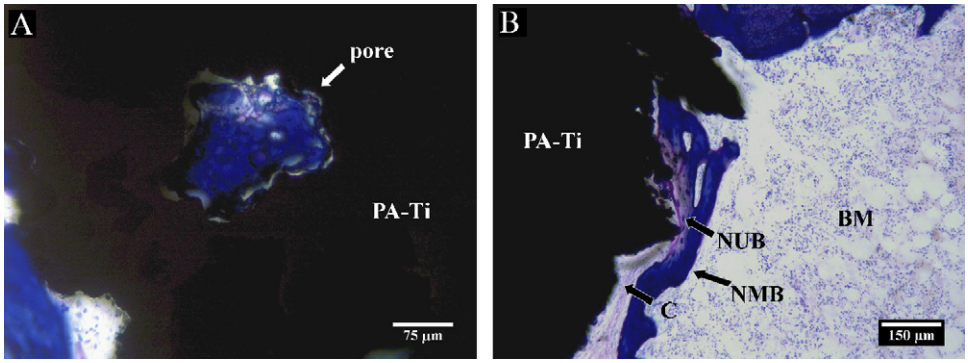

Fig. 11. Images of histological sections of a PA–Ti hybrid implanted in a rat femur after 4 weeks. Non-decalcified, plastic embedded samples were stained with methylene blue and basic fuchsin. Image A shows mineralized bone formation (blue) within an interior pore of the PA–Ti hybrid. Image B shows new bone formation adjacent to and into the PA–Ti hybrid. The location and formation of these bone spicules are evidence of osteoconduction, with new mineralized bone (NMB, deep blue) on the exterior, new unmineralized bone (NUB, pink) in the middle, and collagenous fibers (C) against the PA–Ti hybrid.

4. Conclusions

We have shown that Ti–6Al–4V foams with 52.5% porosity can be filled with a self-assembling peptide amphiphile to create a bioconductive hybrid. SEM showed that the structure of the PA nanofiber matrix is retained when filling the pores of the foam, while confocal microscopy showed that the PA infiltrates the entire thickness. The PA matrix has been shown to mineralize with calcium phosphate, and cells can be encapsulated in these hybrids in a controlled manner. Preliminary in vivo experiments show that de novo bone is formed adjacent to

and inside the PA–Ti hybrid by 4 weeks, offering strong evidence of osteoconduction. Self-assembly of peptide amphiphile nanofibers within pores of metallic foams has potential to induce mineralization and direct a cellular response from the host tissue at its interfaces with an implant.

Acknowledgments

The authors gratefully acknowledge funding support from the National Science Foundation, under Award no. DMR-0505772 and the National Institutes of Health, under Award no. 5R01DE015920. Electron microscopy was performed in the Electron Probe Instrumentation Center (EPIC) facility of the NUANCE Center at Northwestern University, and is supported by NSF-NSEC, NSF-MRSEC, Keck Foundation, the State of Illinois, and Northwestern University. Confocal microscopy was performed in the Biological Imaging Facility (BIF) at Northwestern University. Portions of the cell work were performed in the Institute for Bionanotechnology in Medicine (IBNAM) at Northwestern University. We thank Mr. Ben Myers for his technical help with experiments at EPIC and Dr. William Russin for his technical help with experiments at BIF. We thank Dr. Catherine Ambrose for histological preparation performed at The University of Texas Houston Health Science Center, and Dr. Sue Crawford and Dr. Philip Fitchev at Northwestern University for her help with histological analysis.

References

[1] Sargeant A, Goswami T. Hip implants: Paper V. Physiological effects. Mater Des 2006;27(4):287–307.
[2] Ryan G, Pandit A, Apatsidis DP. Fabrication methods of porous metals for use in orthopaedic applications. Biomaterials 2006;27(13):2651–70.
[3] Long M, Rack HJ. Titanium alloys in total joint replacement—a materials science perspective. Biomaterials 1998;19(18):1621–39.
[4] Mcnamara BP, Toni A, Tayor D. Effects of implant material properties and implant–bone bonding on stress shielding in cementless total hip-arthroplasty. Adv Eng Mater 1995;99-1:309–14.
[5] Wen CE, Mabuchi M, Yamada Y, Shimojima K, Chino Y, Asahina T. Processing of biocompatible porous Ti and Mg. Scripta Mater 2001;45(10):1147–53.
[6] Zardiackas LD, Parsell DE, Dillon LD, Mitchell DW, Nunnery LA, Poggie R. Structure, metallurgy, and mechanical properties of a porous tantalum foam. J Biomed Mater Res 2001;58(2):180–7.
[7] Ayers RA, Simske SJ, Bateman TA, Petkus A, Sachdeva RLC, Gyunter VE. Effect of nitinol implant porosity on cranial bone ingrowth and apposition after 6 weeks. J Biomed Mater Res 1999; 45(1):42–7.
[8] Li HL, Oppenheimer SM, Stupp SI, Dunand DC, Brinson LC. Effects of pore morphology and bone ingrowth on mechanical properties of microporous titanium as an orthopaedic implant material. Mater Trans 2004;45(4):1124–31.
[9] Shen H, Brinson LC. Finite element modeling of porous titanium. Int J Solids Structs 2007;44(1):320–35.
[10] Thelen S, Barthelat F, Brinson LC. Mechanics considerations for microporous titanium as an orthopedic implant material. J Biomed Mater Res Part A 2004;69A(4):601–10.
[11] Davis NG, Teisen J, Schuh C, Dunand DC. Solid-state foaming of titanium by superplastic expansion of argon-filled pores. J Mater Res 2001;16(5):1508–19.
[12] Dunand DC. Processing of titanium foams. Adv Eng Mater 2004; 6(6):369–76.
[13] Li JP, de Wijn JR, Van Blitterswijk CA, de Groot K. Porous Ti6Al4V scaffold directly fabricating by rapid prototyping: preparation and in vitro experiment. Biomaterials 2006;27(8):1223–35.
[14] Queheillalt DT, Choi BW, Schwartz DS, Wadley HNG. Creep expansion of porous Ti–6Al–4V sandwich structures. Metall Mater Trans A 2000;31(1):261–73.
[15] Greiner C, Oppenheimer SM, Dunand DC. High strength, low stiffness, porous NiTi with superelastic properties. Acta Biomater 2005;1(6):705–16.
[16] Lagoudas DC, Vandygriff EL. Processing and characterization of NiTi porous SMA by elevated pressure sintering. J Intelligent Mater Syst Struct 2002;13(12):837–50.
[17] Elzey DM, Wadley HNG. The limits of solid state foaming. Acta Mater 2001;49(5):849–59.
[18] Spoerke ED, Stupp SI. Synthesis of a poly (L-lysine)-calcium phosphate hybrid on titanium surfaces for enhanced bioactivity. Biomaterials 2005;26(25):5120–9.
[19] Li J, Yun H, Gong YD, Zhao NM, Zhang XF. Investigation of MC3T3-E1 cell behavior on the surface of GRGDS-coupled chitosan. Biomacromolecules 2006;7(4):1112–23.
[20] Porte-Durrieu MC, Guillemot F, Pallu S, Labrugere C, Brouillaud B, Bareille R, et al. Cyclo-(DfKRG) peptide grafting onto Ti–6Al–4V: physical characterization and interest towards human osteoprogenitor cells adhesion. Biomaterials 2004;25(19):4837–46.
[21] Harrington DA, Cheng EY, Guler MO, Lee LK, Donovan JL, Claussen RC, et al. Branched peptide-amphiphiles as self-assembling coatings for tissue engineering scaffolds. J Biomed Mater Res Part A 2006;78A(1):157–67.
[22] Hartgerink JD, Beniash E, Stupp SI. Peptide-amphiphile nanofibers: a versatile scaffold for the preparation of self-assembling materials. Proc Natl Acad Sci USA 2002;99(8):5133–8.
[23] Hartgerink JD, Beniash E, Stupp SI. Self-assembly and mineralization of peptide-amphiphile nanofibers. Science 2001;294(5547): 1684–8.
[24] Silva GA, Czeisler C, Niece KL, Beniash E, Harrington DA, Kessler JA, et al. Selective differentiation of neural progenitor cells by high-epitope density nanofibers. Science 2004;303(5662): 1352–5.
[25] Guler MO, Hsu L, Soukasene S, Harrington DA, Hulvat JF, Stupp SI. Presentation of RGDS epitopes on self-assembled nanofibers of branched peptide amphiphiles. Biomacromolecules 2006;7(6):1855–63.
[26] Murray NGD, Schuh CA, Dunand DC. Solid-state foaming of titanium by hydrogen-induced internal-stress superplasticity. Scripta Mater 2003;49(9):879–83.
[27] Murray NGD, Dunand DC. Microstructure evolution during solid-state foaming of titanium. Compos Sci Technol 2003;63(16): 2311–6.
[28] Murray NGD, Dunand DC. Effect of thermal history on the superplastic expansion of argon-filled pores in titanium: Part I kinetics and microstructure. Acta Mater 2004;52(8):2269–78.
[29] Murray NGD, Dunand DC. Effect of initial preform porosity on solid-state foaming of titanium. J Mater Res 2006;21(5):1175–88.
[30] Guler MO, Soukasene S, Hulvat JF, Stupp SI. Presentation and recognition of biotin on nanofibers formed by branched peptide amphiphiles. Nano Lett 2005;5(2):249–52.
[31] Allen R, Eisenberg S, Gray M. Tissue engineering methods and protocols. Totowa, NJ, USA: Humana Press; 1999.
[32] Kim YJ, Sah RLY, Doong JYH, Grodzinsky AJ. Fluorometric assay of DNA in cartilage explants using Hoechst-33258. Anal Biochem 1988;174(1):168–76.
[33] Kearns M, Blenkinsop P, Barber A, Farthing T. Metals and Materials. 1987; 3(2): 85.

[34] Kearns MW, Blenkinsop PA, Barber AC, Farthing TW. Manufacture of a novel porous metal. Int J Powder Metall 1988;24(1):59–64.
[35] Schwartz DS, Shih DS, Lederich RJ, Martin RL, Deuser DA. Development and Sacle-up of the low density core process for Ti-64. Mat Res Soc Symp Proc 1998;521:225–30.
[36] Gibson LJ, Ashby MF. Cellular solids. 2nd ed. Cambridge: Cambridge University Press; 1997.
[37] Ratner BD. Biomaterials science: an introduction to materials in medicine. 2nd ed. Amsterdam, Boston: Elsevier Academic Press; 2004.
[38] Itala AI, Ylanen HO, Ekholm C, Karlsson KH, Aro HT. Pore diameter of more than 100 mu m is not requisite for bone ingrowth in rabbits. J Biomed Mater Res 2001;58(6):679–83.
[39] Emans N, Biwersi J, Verkman AS. Imaging of endosome fusion in Bhk fibroblasts based on a novel fluorometric avidin–biotin binding assay. Biophys J 1995;69(2):716–28.
[40] Green NM. Avidin. Adv Protein Chem 1975;29:85–133.
[41] Nicol F, Nir S, Szoka FC. Orientation of the pore-forming peptide GALA in POPC vesicles determined by a BODIPY–avidin/biotin binding assay. Biophys J 1999;76(4):2121–41.